PERGAMON

Journal of Structural Geology 23 (2001) 1241–1254

JOURNAL OF STRUCTURAL GEOLOGY

www.elsevier.nl/locate/jstrugeo

Joint nucleation in layered rocks with non-uniform distribution of cavities

Ram Weinberger*

Geological Survey of Israel, 30 Malkhe Israel St., Jerusalem 95501, Israel

Received 22 March 2000; accepted 25 October 2000

Abstract

Characterization of 'critical flaws' that initiate into systematic joints is essential for understanding the process of fracturing in sedimentary rocks. In this study, advantage is taken of the well-developed surface morphology of joints in the dolomite layers of the Judea Group, central Israel, and the role played by spherical cavity-shaped flaws during nucleation and growth of joints is analyzed. An analysis of cavity geometry and distribution reveals that joint initiation points are governed by such isolated, relatively large cavities, preferably located close to the bedding top and by stress gradients during joint nucleation. In the absence of macroscopic cavities, joint initiation points are located along bedding interfaces. Consequently, joints typically show two forms of growth, depending on the abundance and spatial distribution of cavities within the layers. In layers with plentiful cavities, joints preferably nucleate at critical cavities, propagate vertically toward the bedding interfaces and horizontally toward adjacent joints, and form elliptical fractures. In layers free of cavities, joints nucleate at bedding interfaces, commonly propagate downward toward the layer base and adjacent joints, and form semi-elliptical fractures. In both cases, bedding interfaces between the dolomite layers impedes joint propagation. Fractographic methods based on joint surface morphology yield satisfactory, first-order estimates of the driving paleostress required to initiate joints in the Judea Group. © 2001 Elsevier Science Ltd. All rights reserved.

1. Introduction

Field observations indicate that nucleation and growth of joints in sedimentary rocks are strongly related to inhomogeneity and layer discontinuities of the strata. In the layered siltstones and shales of the Appalachian Plateau, central New York, joint initiation points are almost always located at bedding interfaces at flaws such as fossil inclusions, pyrite concretions, voids, cusps and burrows along such surfaces (Bahat and Engelder, 1984; Helgeson and Aydin, 1991; Lacazetta and Engelder, 1992). When a stack of siltstone layers is jointed, the joint initiation points are all located at the top of each layer, consistently where a joint approaching from above first intersects the next layer (Helgeson and Aydin, 1991). In stratified mud, the mudcrack initiation points are consistently located along or near the base of the desiccated sediment, where potential flaws (e.g. long grain boundaries) are more abundant because of the natural fining-upward sorting of grains (Weinberger, 1999, 2000). Consequently, these large flaws become critical before small flaws at the top (e.g. short grain boundaries), even though the tensile stress caused by drying declines downwards through the mud. Other cracks commonly nucleate at the middle or upper part of layers under lateral extension or bending (Bahat, 1991). These observations suggest that the location of joint initiation points is governed by several factors, including flaw distribution and geometric characteristics, rock and interface properties, and loading conditions.

Several studies have pointed out that joint growth is disrupted by bedding interfaces, and that joints are selectively confined to certain layers (i.e. single-layered joints), commonly with differing orientation, spacing, and surface morphology (e.g. Becker and Gross, 1996). Joints from adjacent layers, however, may communicate across interfaces, typically forming an overall composite joint with out-of-plane arrangement (Helgeson and Aydin, 1991). In other cases, several layers are fractured together by multilayered joints that cross bedding interfaces (Bahat, 1991). One important reason to study joint-set architecture is that the physical continuity of joints from one layer to another has a profound effect on fluid migration (Caine and Forster, 1999). Constraints on the geometry of fractured rocks may be obtained by documenting the three-dimensional structure of joint systems.

The strength of brittle solids is predicated on the existence of flaws. These flaws range from 1 μm (high-density, fine-grained, polycrystalline ceramic) to 1 mm and above (concretes, rocks), and occur in both the surface and the

* Fax: +972-2-5380-688.
E-mail address: rami@earth.es.huji.ac.il (R. Weinberger).

0191-8141/01/$ - see front matter © 2001 Elsevier Science Ltd. All rights reserved.
PII: S0191-8141(00)00192-9

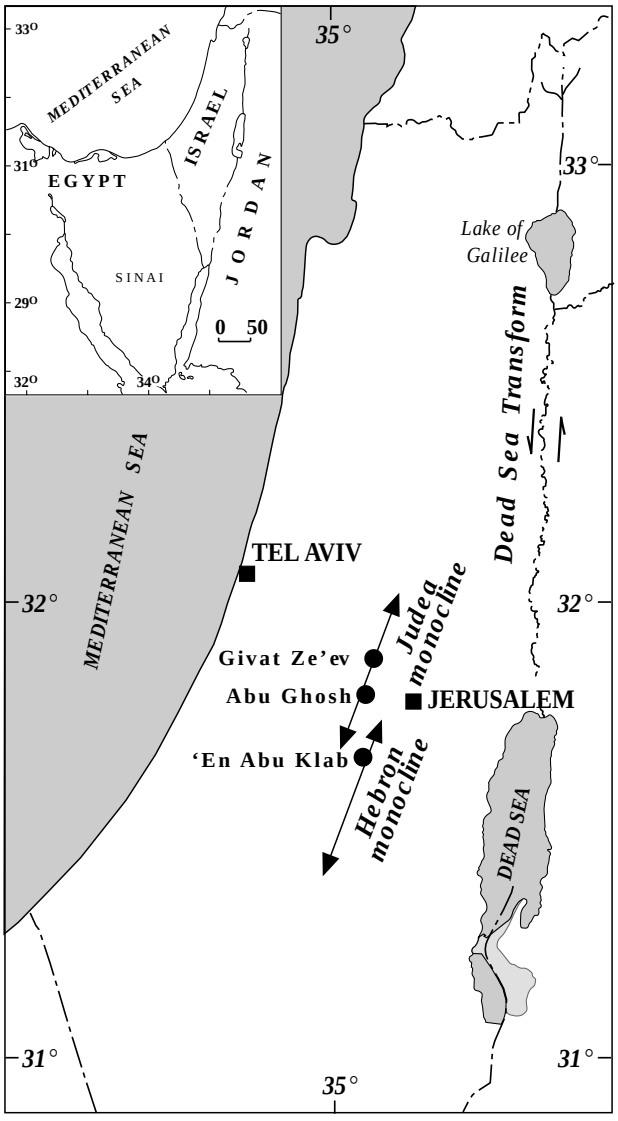

Fig. 1. Location map of the study areas. Axes of the Judea and Hebron monoclines are schematically indicated.

bulk material. Almost invariably, the defects introduced during material processing and rock formation are widely distributed in size, shape, orientation and location, forming bimodal or even multimodal 'flaw populations' (Lawn, 1993, pp. 307–309). In rocks, it is likely that more than one flaw type coexists (Wong and Zhu, 1999) but geologists are usually more concerned with the 'worst flaws' or 'critical flaws' that initiate into systematic joints. Some of the more common macroscopic flaw types in rocks are cavity and inclusion populations. Critical cavities and inclusions are rarely characterized in natural conditions, however, although such analysis is essential for understanding the process of fracturing in rocks, and the mechanics of fracture network formation (Renshaw, 1996).

The orientation and geometry of joints are also attractive subjects for structural analysis, because they may be used to infer the state of the prevailing stress when joint systems formed (Engelder and Geiser, 1980; Pollard and Aydin, 1988; Olson and Pollard, 1989). Such analysis can greatly benefit from fractography, the study of fracture processes through examination of surface morphology of joints (Bahat, 1991). In this study, advantage is taken of the well-developed surface morphology of joints in the Soreq Formation, Judea Group (Arkin and Hamaoui, 1967; Upper Cretaceous, central Israel; Fig. 1), which uniquely records the history of fracture nucleation and growth in layered rocks. This morphology, commonly termed 'plumose structure', consists of a joint initiation point and concentric undulations (rib markings) that radiate from the origin toward the peripheries of the crack planes. Fine surface relief features, known as hackle lines, form parallel to the local propagation direction and perpendicular to the rib markings (Fig. 2). These structures have been used as a powerful field tool for studying fracture processes in rocks and sediments (Bankawitz, 1966; Kulander et al., 1979; DeGraff and Aydin, 1988; Bahat, 1991; Ameen, 1995; Weinberger, 1999), and to help estimate the local paleostresses which cause fracture initiation (i.e. 'fracture stress', Bahat and Rabinovitch, 1988). In this study, this tool is utilized to elucidate the role of macroscopic flaw distribution, shape and size on the nucleation mechanisms of joints in natural conditions, and to examine the effect of bedding interfaces on joint growth and arrangement. Using published rock mechanics data, the applicability of the fractographic methods for estimating the fracture stress of joint sets in layered rocks is further evaluated, and the associated state of stress encountered by the strata at the time of fracturing is constrained.

2. Joints in the Soreq Formation

The Cenomanian Soreq Formation typically consists of a stack of dolomite layers, ranging in thickness between 0.4 and 3 m, partitioned by very thin interbedded marl films (Fig. 3). Numerous cavities and some quartz geodes are found in the dolomite layers. They are non-uniformly distributed and vary in size and shape within individual layers and among layers. The quartz geodes contain inclusions of anhydrite and are thus generally believed to be replacement products of anhydrite nodules (Sass and Bein, 1978). The formation of both the cavities and the geodes is related to hypersaline water that permits early diagenetic growth of anhydrite nodules. Under certain conditions, marine-derived water dissolves the anhydrite nodules; this would account for the cavities observed in the dolomite layers. If the water is rich in silica, the nodules are filled by quartz, generating the observed geodes.

Two systematic joint sets fracture the dolomite layers at approximately W-striking and NNW-striking directions (Fig. 4). Cross-cutting relations indicate that the NNW-striking joints are younger than the W-striking joints. Since the W-striking set is the oldest in the studied

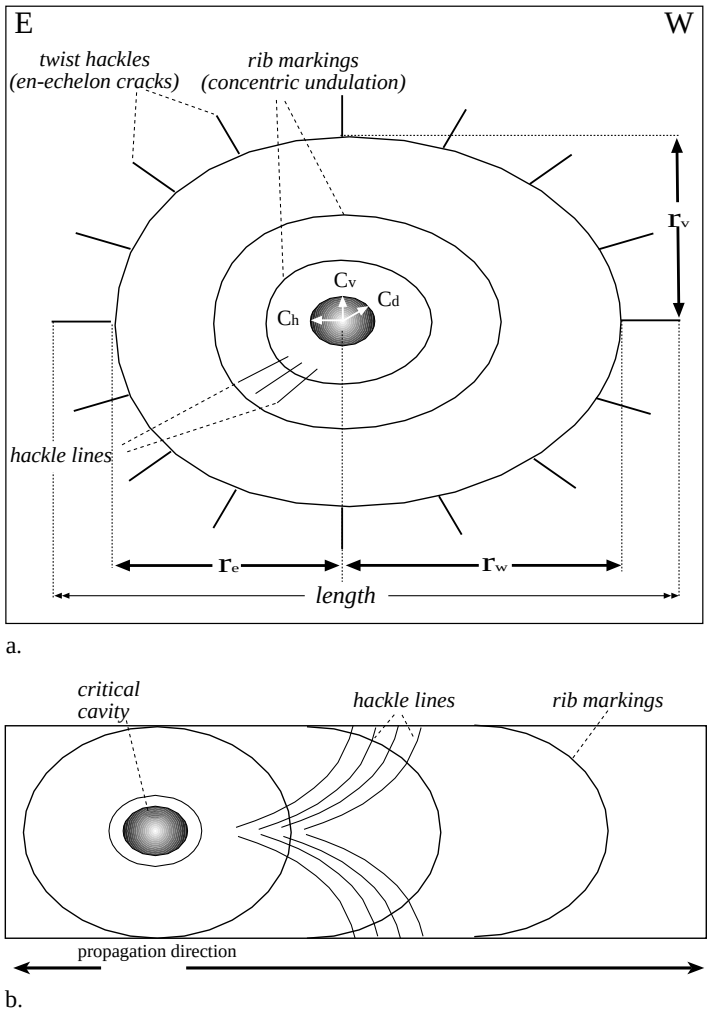

Fig. 2. Schematic illustration of a fracture surface showing characteristic geometric features. (a) Rib markings (concentric undulations) and hackle lines radiated from a flaw (critical cavity). The distances from the center of the critical cavity up to the rougher region of twist hackles are measured westward (r_w), eastward (r_e), and upward (r_v) along the W-striking joints. The distances C_h and C_v are the horizontal and vertical semi-axis of a critical cavity-shaped flaw, respectively, and C_d is the joint-normal semi-axis. The horizontal length of the joint is indicated. (b) Rib markings with approximately similar curvature. Hackle lines are everywhere perpendicular to the rib markings and parallel to the local propagation direction. Overall propagation direction is indicated.

localities, its formation is not influenced by the NNW-striking set. The association between the W-striking joints and cavities in the Soreq Formation were studied in several localities around Jerusalem (Fig. 1), including roadcuts along the highway between Tel-Aviv and Jerusalem near Abu Ghosh village (31°48′N/35°07′E), the spring 'En Abu Klab (31°40′N/35°07′E), and a site west of Givat Ze'ev (31°52′N/35°08′E). The latter site is the most remarkable one and is studied in detail below.

The horizontal layers of the Soreq Formation lie close to the axis of the Judea monocline (Fig. 1). The W-striking joints are arranged en échelon and are selectively confined to certain layers (single-layer joints). Offsets are between 0.15 and 0.3 m and overlap between 0 and 0.2 m (Fig. 3). Three types of plumose structures can be identified based on the layer characteristics. Type 1 consists of circular-to-elliptical rib markings and is formed in layers with plentiful cavities ('cavity-rich layers') (Fig. 3, Layer 1; Fig. 5). The associated joints preferably nucleate at cavities and propagate vertically toward the bedding interfaces and horizontally toward adjacent joints, forming circular-to-elliptical fractures (Fig. 6c). The horizontal semi-axis of the elliptical fracture is generally the major semi-axis. The lower and upper vertical terminations of a joint are intersections between the joint and the bedding interfaces. In Layer 1, however, the lower terminations are not always well defined because a fracture surface morphology is obscured by the cluster of cavities at the layer base (Fig. 6c). The lateral terminations of a joint are blind, where pairs of closely spaced joints overlap along straight paths.

The Type 2 plumose structure consists of semi-circular-to-semi-elliptical rib markings and is formed only in 'cavity-free layers' (Fig. 3, Layer 7; Fig. 6a). The associated joints nucleate at bedding interfaces and propagate downward toward the layer base and adjacent joints, forming semi-circular-to-semi-elliptical fractures. Terminations are

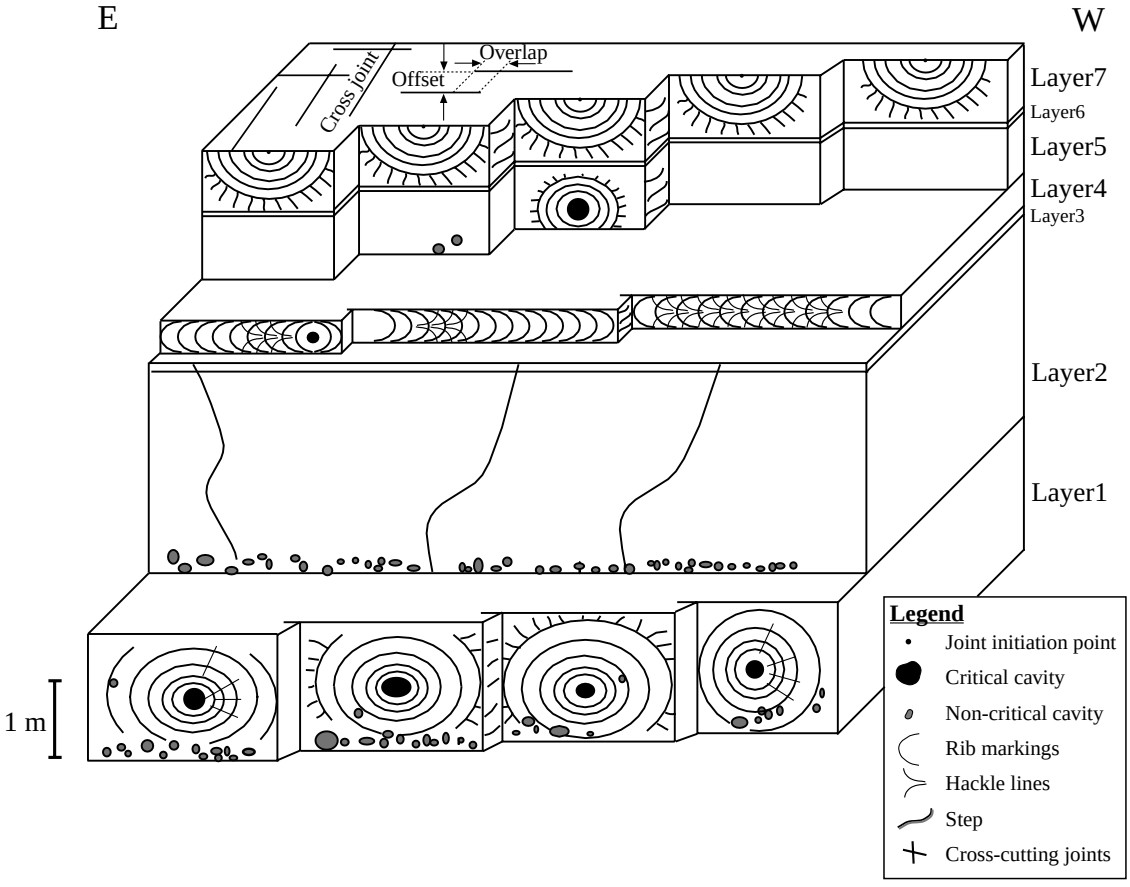

Fig. 3. Graphic representation of the outcrop west of Givat Ze'ev displaying arrays of joints with diagnostic surface morphologies. Joints are selectively confined to certain layers, commonly with differing fracture surface morphology. Layer 2 and Layer 3 are not fractured by a systematic joint set. Gray ellipses represent non-critical cavities; black ellipses represent critical cavities. Cross-joints (Fig. 4) and definition of 'overlap' and 'offset' are indicated at the top of Layer 7.

similar to that of joints in cavity-rich layers. Type 3 consists of rib markings with approximately similar curvature and is formed in relatively thin layers (<0.4 m) (Fig. 3, Layer 4; Fig. 6b). The associated joints preferably nucleate at the middle of the thin layers, but are not necessarily associated with macroscopically discernable cavities. Their horizontal length is several times larger than their height, which is approximately the layer thickness (Fig. 6b).

3. Features of 'critical cavities'

3.1. General

Cavities associated with joint nucleation are termed hereafter 'critical cavities' and their respective fractures are termed 'cavity-driven joints'. The cavity horizontal semi-axis, C_h, and vertical semi-axis, C_v, are measured from the center of a cavity to its periphery, defined by the intersection of the respective fracture plane and the cavity rim (Fig. 2). The cavity 'depth', C_d, is measured from the center of the cavity to its rim normal to the fracture plane (Fig. 2b). The characteristic size of a cavity, Z, is defined as the mean of C_h and C_v. Fourteen adjacent critical cavities in Layer 1, one in Layer 5, and five in Layer 7 and their associated joints were carefully measured for the present analysis (Table 1). For comparison, all cavities along an 8-m-long traverse in Layer 1, including six critical cavities and 58 non-critical cavities, were also studied in detail. Fig. 7 shows the resulting measurements of cavity shape, size and location within the layer. An additional interdependent variable, the degree of isolation, can be derived from these measurements. These variables are analyzed below in an attempt to characterize features of flaw criticality.

3.2. Shape

Critical cavities are approximately spherical, with $C_h = 45 \pm 20$ mm, $C_v = 43 \pm 20$ mm, $C_d = 45 \pm 23$ mm, and in-plane $C_h/C_v \approx 1$ ratios (Table 1). Non-critical cavities are also approximately spherical, with $C_h = 35 \pm 27$ mm, $C_v = 30 \pm 23$ mm, and $C_d = 32 \pm 23$ mm (Fig. 8a). Noticeably, several eccentric cavities ($C_h/C_v \approx 2$) appearing close to the base of Layer 1 are non-critical, e.g. an ellipsoidal cavity at distance 4.40 m along the traverse (Fig. 7). If a cavity deviates from a perfect

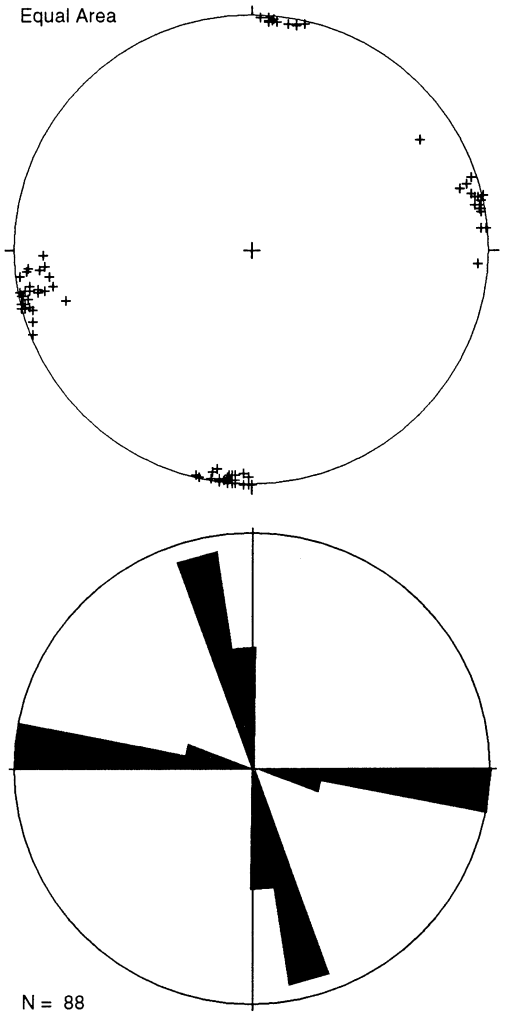

Fig. 4. Upper hemisphere stereographic projection of poles to fracture planes and rose diagram of joint orientation in the Soreq Formation. Sector length is proportional to number of joints.

sphere, the major semi-axis commonly coincides with C_h. This is particularly the case for critical cavities, where only in one case the difference between C_v and C_h is larger than 3 mm (Table 1).

3.3. Size

The mean characteristic size of all critical cavities ($Z = 44$ mm) is larger than that of non-critical cavities ($Z = 33$ mm). More details are gained from histograms of cavity sizes in Layer 1 (Fig. 8b). The frequency of critical cavities is different from that of all cavities; relatively small and very large cavities are not associated with joint initiation. Indeed, no critical cavity is among the top five largest and the fifteen smallest cavities (Table 1).

3.4. Location within layer

To test the null hypothesis that cavities (critical and non-critical) are randomly distributed with Layer 1, the section presented in Fig. 7 was divided into 48 area units of 0.5×0.5 m^2 each, and the number of cavities in each unit counted. This procedure provided the observed data for a standard Chi-square test on this cavity population, and helped to calculate the expected data based on a Poisson distribution (Davis, 1973), with λ equal to the mean size of all cavities. The test concluded that the null hypothesis should be rejected at 95% confidence. Thus, cavity distribution is non-random, reflecting the tendency of cavities to be more abundant toward the layer base. Additionally, of all cavities, critical cavities are generally located closest to the top of the layer. Only 5 out of 58 non-critical cavities are located more closely to the top of the layer than the critical cavities (Figs. 7 and 8c). In addition, all five are smaller in size than the smallest critical cavity (Table 1, Cavity 10).

3.5. Isolation

For each cavity, the distance, D_j, was measured from the center of cavity j to the center of the in-plane nearest neighbor, and the number of neighbors S_i within a radius of 0.5 m around the center of cavity j was counted. The dimensionless index of in-plane isolation for cavity j, I_j, is defined by:

$$I_j = \frac{D_j}{Z_j} \frac{1}{S_j + 1}. \quad (1)$$

A high isolation index implies a large distance to the nearest neighbor and a limited number of neighbors. The results indicate that the isolation indices of critical cavities are typically one order of magnitude greater than those of non-critical cavities (Fig. 8d), i.e. critical cavities are much more isolated than most of the non-critical cavities. Noticeably, several isolated cavities appearing close to the base of Layer 1 are non-critical, e.g. a small cavity at distance 6.00 m along the traverse (Fig. 7).

4. Estimation of paleostress

4.1. General

Joints in the Soreq Formation allow the estimate of the state of stress in the strata at the time of the nucleation of W-striking joints. This strike direction indicates that the remote horizontal least compressive stress (σ_1^r) was oriented N–S, because joints grow along planes that are perpendicular to least compressive principal stress (Engelder and Geiser, 1980). To constrain the magnitude of σ_1^r, the associated fracture stress utilizing the two fractographic methods presented in the next section were estimated first. Then, the magnitude of σ_1^r was calculated, based on the relations between the remote stress and the stress amplification associated with a circular hole (e.g. Jaeger and Cook, 1979).

4.2. Fractographic methods

Two fractographic methods used in ceramics and glass

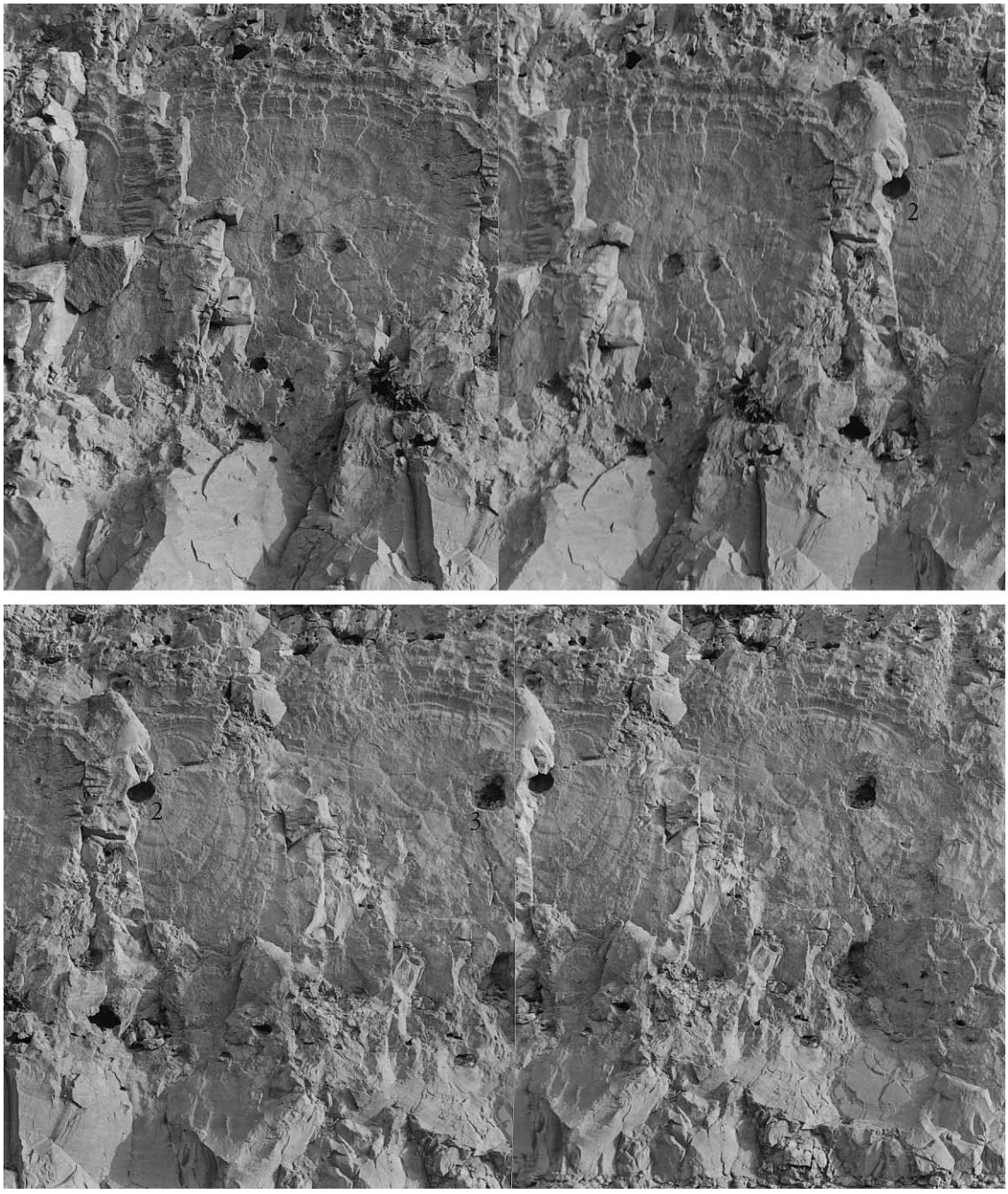

Fig. 5. Two pairs of stereoscopic photographs illustrate the three dimensional structure of cavity-driven joints in Layer 1. Joints occasionally consist of concentric rib markings close to the critical cavity and elliptical rib markings away from it. Large, nearly radial, twist hackles in joint 1 indicate that a local mixed-mode loading (mode I + III) was imposed on the joint plane. Offsets, or stereoscopically, the "depth" of steps, are between 0.2 and 0.3 m.

were adapted by Bahat and co-workers (Bahat and Rabinovitch, 1988; Bahat, 1998; Bahat et al., 1999) for estimating the fracture stress in rock masses. The methods utilize a direct relation between fracture geometry and stress. The first method is based on the r to C_{cr} ratio, where C_{cr} is the critical flaw radius, when spontaneous propagation starts, and r is the distance from the center of the critical flaw up to the rougher region of twist hackles (en échelon cracks) (Fig. 9). The method assumes that r/C_{cr} is a rock property, and uses empirical values determined for ceramics ($r/C_{cr} = 16.7$) and glass ($r/C_{cr} = 13.9$) to calculate C_{cr} for a measured r (Bahat and Rabinovitch, 1988 and references therein). In order to constrain the fracture stress, σ_f, the mode I stress intensity factor at which the crack starts to propagate critically (K_{Ic}, fracture toughness) and C_{cr} are substituted into the following empirical relation:

$$\sigma_f = K_{Ic}\left[Q/\left(1.2\pi C_{cr}\right)\right]^{1/2} \quad (2)$$

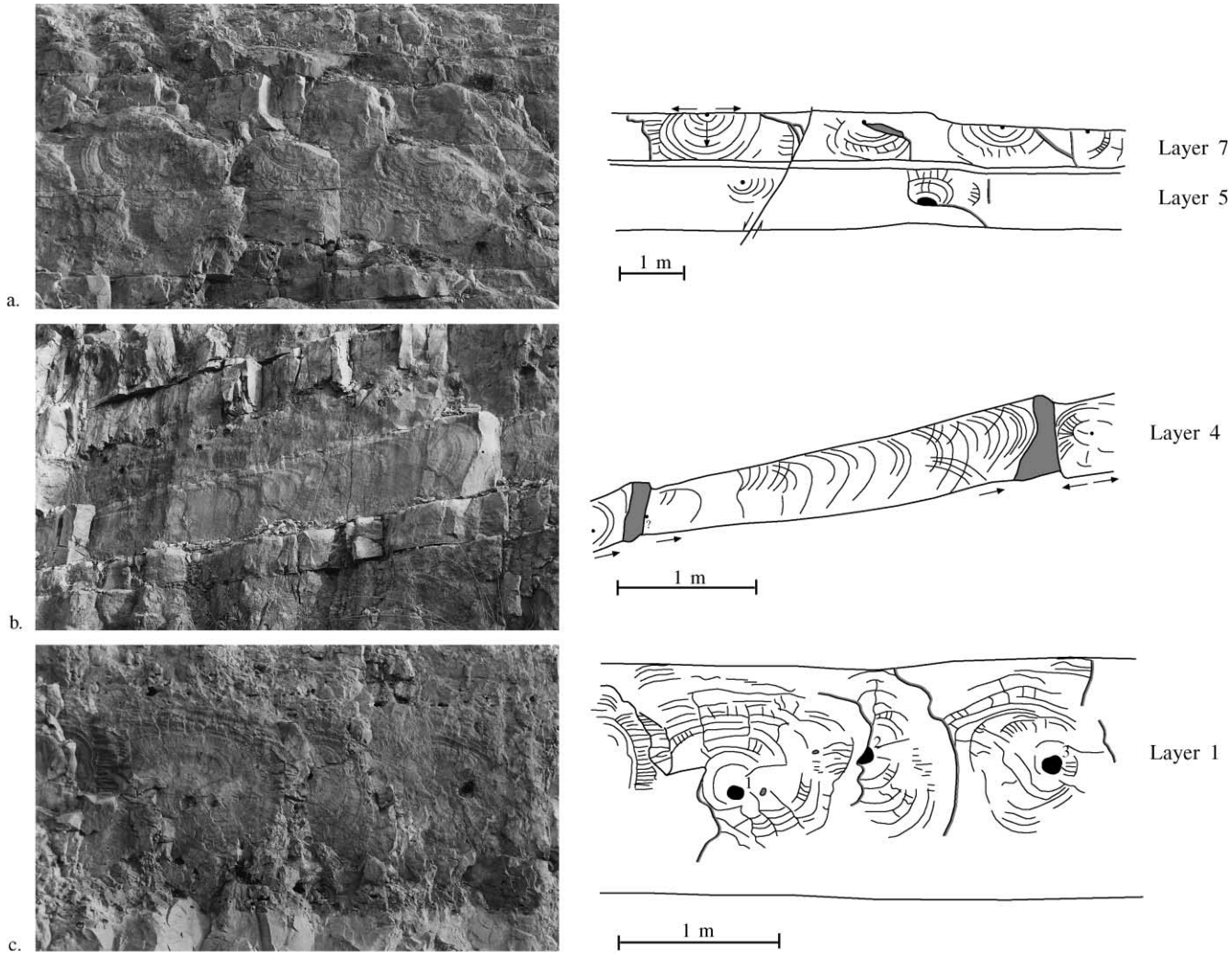

Fig. 6. Photographs and surface-morphology interpretation of joints in the Soreq Formation. Joints seldom cross bedding interfaces. (a) View of Type 1 (Layer 5) and Type 2 (Layer 7) plumose structures. Joint initiation points at Layer 5 are commonly located within the layer and at Layer 7 along the upper part of the layer. A small fault is younger than the joints. (b) Side view of Type 3 plumose structure in Layer 4. Joint initiation points is located within the layer. (c) View of Type 1 plumose structures in Layer 1. Three adjacent joints and their associated critical cavities are indicated. Numbers near critical cavities refer to cavities in Fig. 7. Arrows indicate propagation directions. See also legend in Fig. 3.

where Q is a modifying geometric factor ranging in value from 1.0 for a long shallow flaw to 2.46 for a semi-circular flaw.

The second method for calculating the fracture stress (Bahat and Rabinovitch, 1988) directly applied the distance r (Fig. 9) utilizing the expression:

$$\sigma_f = 2G(E\gamma/\pi r)^{1/2} \quad (3)$$

where E is Young's modulus, γ is the surface energy, and G is the enhancement factor, varying between 22 and 52. Estimates of these constants yield σ_f from Eq. (3). The fractographic methods are most adequately applied to estimate the stress associated with the initiation of a single joint in an otherwise homogeneous material. The limitations of these methods for the case of jointing in layered rocks are addressed in Section 5.2.

4.3. Dimensions of cavity-driven joints

The fractographic methods are based on direct measurements of joint dimensions. For the present analysis, several variables are defined to characterize the dimensions of cavity-driven joints (Fig. 2). The vertical distance r_v from the center of a critical cavity up to the rougher region of twist hackles is measured along a vertical line through the cavity center. Similarly, the horizontal distances r_w and r_e from the center of a critical cavity up to the rougher region of twist hackles are measured westward (r_w) and eastward (r_e) along a horizontal line through the cavity center. The distance r_h is taken as the maximum distance between r_w and r_e. The average value of r_h is 0.62 ± 0.23 m, and that of r_h/C_h ratios is 14.0 ± 5.4 (Table 1). It is assumed that r_h provides the best estimate for r in Eqs. (2) and (3), because it is less affected by bedding interfaces than the vertical

Table 1
Summary of field measurements

Layer no.	Joint no.[a]	Cavity semi-axis (mm)			Distance r (m)		r_h/C_h	Bed thickness (m)	Distance from bottom (m)
		C_h	C_v	C_d	r_h[b]	r_v[c]			
Layer 1	1	55	50	35	0.64	0.61	11.7	1.55	0.72
	2	57	47	45	0.36	0.24	6.3	1.53	1.05
	3	62	65	75	0.51	0.35	8.2	1.57	0.90
	4	75	75	70	0.90	0.44	12.0	1.60	0.66
	5	40	40	50	0.63	0.59	15.7	1.64	0.66
	6	35	27	35	0.59	0.50	17.0	1.61	0.95
	7	75	75	90	0.80	0.54	10.7	1.52	0.78
	8	40	40	55	0.41	0.53	10.2	1.51	0.90
	9	35	30	50	0.77	0.40	22.1	1.60	0.97
	10	15	15	10	0.38	0.40	25.6	1.54	1.07
	11	52	55	60	0.89	0.39	17.1	1.45	0.84
	12	15	22	10	0.14	0.31	9.6	1.52	1.05
	13	52	17	40	0.90	0.33	17.2	1.68	1.00
	14	60	50	30	0.76	0.43	12.6	1.60	0.95
Average		45	43	46	0.62	0.44	14.0		
SD		20	20	23	0.23	0.12	5.4		
Median		52	43	47	0.63	0.42	12.3		
Layer 5	1	85	45	45	0.51	0.35	–	0.81	0.30
Layer 7	1	–	–	–	0.80	0.55	–	0.75	0.75
	2	–	–	–	0.45	0.50	–	0.70	0.70
	3	–	–	–	0.67	0.70	–	0.80	0.80
	4	–	–	–	0.45	0.38	–	0.60	0.60
Average					0.59	0.53			
SD					0.17	0.13			
Median					0.56	0.52			

[a] Joints 7–14 are out of the range of the traverse in Fig. 7.
[b] r_h is the maximum distance between r_w measured westward and r_e measured eastward.
[c] r_v is measured upward in Layer 1 and Layer 5, and downward in Layer 7.

distance r_v. In several cases, however, the r_h/r_v ratios are larger than 1.5 (Table 1). Noticeably, the ratios of cavity spacing to joint length are about 1 (Fig. 7).

4.4. Local fracture stress

The first fractographic method calculates the fracture stress from an empirical relation (Bahat and Rabinovitch, 1988). For each joint in Layer 1, the critical flaw radius C_{cr} is calculated by substituting $r = r_h$ into the constants $r/C_{cr} = 16.7$ and $r/C_{cr} = 13.9$. C_{cr} ranges between 21 and 54 mm. The fracture toughness for the studied dolomite is not known at the present time. A range of values for dolomites/dolostones is quoted by Atkinson and Meredith (1987), ranging from 1.66 MPa $m^{1/2}$ for Kankakee and Falkirk dolostones and 2.47 MPa $m^{1/2}$ for Romeo dolostone. Substituting these extreme values and $Q = 2.46$ (Eq. (2)) yields a fracture stress between ∽5 MPa (largest C_{cr} and smallest fracture toughness) and ∽13 MPa (smallest C_{cr} and largest fracture toughness), where tensile stress reckoned positive (Table 2). Empirical values of r/C_{cr} are within the range of r_h/C_h ratios calculated from direct field measurements in Layer 1 (Table 1), implying that C_h provides a first-order approximation of C_{cr}. Estimates of fracture stress in Layer 5 and Layer 7 yield similar values (Table 2).

The second fractographic method calculates the fracture stress directly from measurements of r_h (Bahat and Rabinovitch, 1988). Young's modulus for the tensile regime and the surface energy for the studied dolomite have not been determined yet. For the present analysis, known values for a comparable carbonate rock, Indiana Limestone, were utilized, with $E = 30$ GPa in the tensile regime (Weinberger et al., 1994), $\gamma = 32$–44 J m^{-2} (Friedman et al., 1972), and G between $2\sqrt{2}$ and $5\sqrt{2}$. For each joint, substituting these values and the measured distance r_h in Eq. (3) yields a fracture stress between ∽3 MPa (smallest surface energy and largest r_h) and ∽15 MPa (largest surface energy and smallest r_h) (Table 2). Fracture stress estimates in Layer 5 and Layer 7 are similar (Table 2). Noticeably, the fractographic estimates are similar to the uniaxial tensile strength of the Soreq Formation, which is between 5.4 and 11.6 MPa (Arkin, 1989).

4.5. Remote stress

The estimated fracture stress, σ_f, helps to constrain the remote stress at the time of fracturing. It is assumed that this stress is equal to the tangential stress along the periphery of

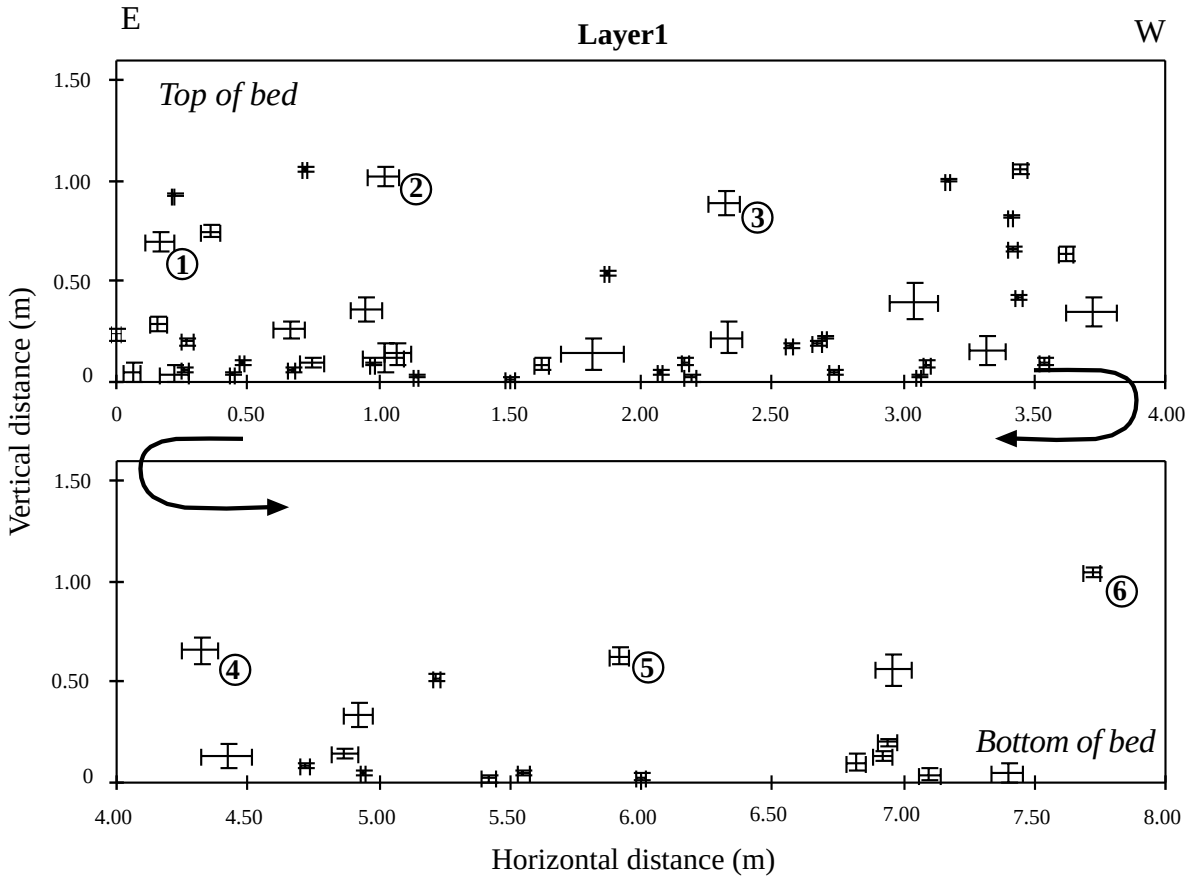

Fig. 7. Representative distribution and dimensions of cavities in Layer 1 (Figs. 3 and 6c) along an 8 m E–W traverse. The small steps along the traverse (Fig. 3) are not indicated. Bars represent the in-plane axes of the ellipsoidal cavities. Cavity centers are located at the intersections of the bars. Numbers denote critical cavities that are associated with joint nucleation (see Table 1).

a circular hole at an infinite region. The general solution for an elliptical hole subjected to biaxial stresses at infinity is given by Jaeger and Cook (1979, pp. 267–269). For a circular hole, the solution is reduced to the simple form:

$$\sigma_f = p_1 + p_2 + 2(p_1 - p_2)\cos(2\beta - 2\eta) \quad (4)$$

where the principal stress p_2 is inclined at β to Ox, p_1 at $\pi/2 + \beta$, and η is the elliptic coordinate (Fig. 10a). Three simple cases of either: (1) uniaxial remote tension, (2) uniaxial remote compression, and (3) biaxial stresses are considered.

Case I: If $p_1 = 0$ and $\beta = \pi/2$, $\sigma_f = 3p_2$ at the end A ($\eta = 0$) (Fig. 10b). For $p_2 = \sigma_1^r$, the uniaxial remote tension, the tangential tension at A is amplified by a stress concentration factor (SCF) 3.0 (e.g. Pollard and Aydin, 1988, p. 1195). The calculated fracture stress was between ∽3 and ∽15 MPa (Section 4.4), suggesting that σ_1^r was one third of these values between ∽1 and ∽5 MPa.

Case II: If $p_1 = 0$ and $\beta = 0$, $\sigma_f = -p_2$ at the end A ($\eta = 0$) (Fig. 10c). For $p_2 = \sigma_3^r$, the uniaxial remote compression, this stress induces tangential tension of the same magnitude at A. For the calculated fracture stress, σ_3^r was between −3 and −15 MPa.

Case III: If $p_1, p_2 \neq 0$ and $\beta = 0$, $\sigma_f = 3p_1 - p_2$ at the end A ($\eta = 0$) (Fig. 10d). For the simple case of pure shear, $p_1 = -p_2$, $\sigma_f = 4p_1$ at the end A. For the calculated fracture stress, the remote tension $p_1 = \sigma_1^r$ was between ∽0.75 and ∽3.75 MPa.

It is likely that the boundary condition at the cavity periphery had been that of constant internal pressure, p. This case may be obtained by superposing the solution for biaxial stresses (Eq. (4)) on the simple solution for constant pressure, p, in a circular hole (i.e. adding p to the right-hand side of Eq. (4); Jaeger and Cook, 1979, p. 269). Consequently, the remote stress in *Case II* could be even less compressive than calculated, and the magnitude of the remote tension in *Cases I* and *III* could be lower than indicated.

5. Discussion

5.1. Nucleation of joints

The remarkably well-exposed outcrops of the Soreq Formation provide a unique opportunity to characterize the populations of critical and non-critical cavity-shaped flaws. Naturally, the population of the non-critical cavities

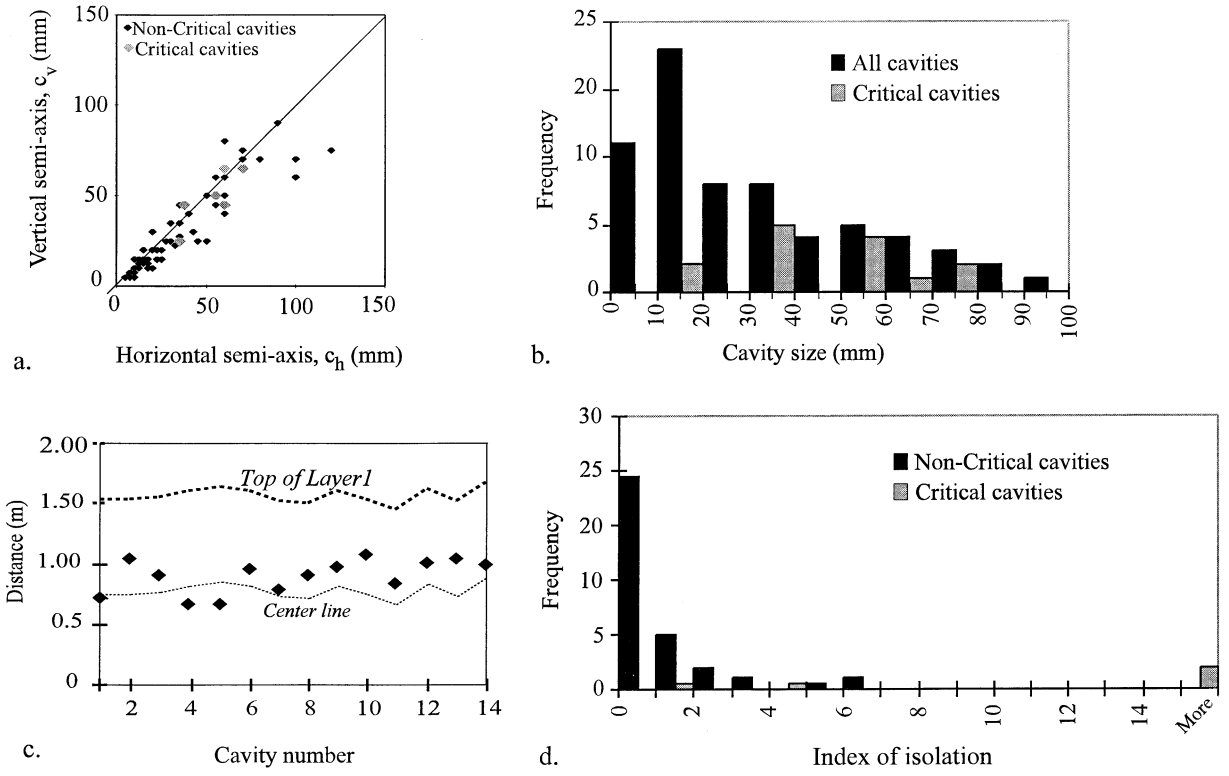

Fig. 8. Analysis of cavity shape, size, and distribution in Layer 1. (a) In-plane horizontal versus vertical semi-axes of critical (gray) and non-critical (black) cavities along an 8 m E–W traverse in Layer 1 (Fig. 7). (b) Histograms of sizes of critical (gray) and non-critical (black) cavities in-plane 1. (c) Origin location of 14 cavity-driven joints with respect to the local layer thickness (see Table 1). (d) Histograms of isolation indices of critical (gray) and non-critical (black) cavities along an 8 m E–W traverse, Layer 1 (Fig. 7).

consists of larger data than that of critical cavities, but their characterization is based on our recognition that both populations contain enough data to allow reliable calculation of statistical variables. Features of these populations are strongly related to diagenetic sedimentary processes (intrinsic controls), which influence cavity geometry (shape, size, orientation) and distribution (isolation, location within layer). The location of joint initiation points, however, depends not only on the intrinsic controls but also on the loading conditions at the time of failure (extrinsic controls). The relative importance of these controls in the nucleation of the joints is assessed below.

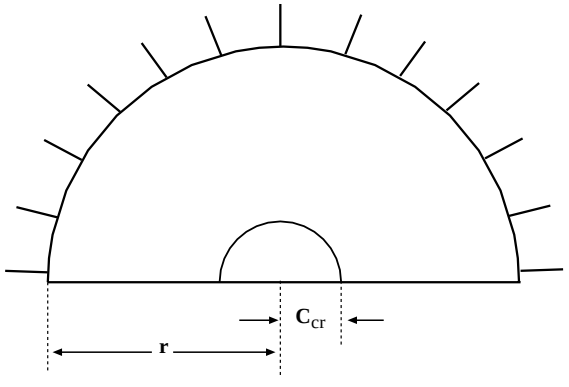

Fig. 9. Schematic of an idealized semi-circular fracture surface. Critical flaw half-length C_{cr} is indicated.The radius r is the distance from the center of the critical flaw up to the rougher region of twist hackles (after Bahat and Rabinovitch, 1988).

The cavity shape plays a minor role in governing the joint initiation points in the Soreq Formation, simply because most cavities are approximately spherical. A few isolated cavities appearing close to the layer base and having eccentric shape with ratios up to two are non-critical (e.g. at distance 1.8 m along the traverse, Fig. 7), although the stress concentration factor (SCF) of cavities with eccentric shape can be much higher than the SCF of spherical cavities (Lawn, 1993, p. 3). In the present case study, this discrepancy suggests that the remaining controls are more important than the cavity shape in governing the joint initiation points.

The cavity size has a noticeable influence on the joint initiation points, because the frequency of critical cavities differs significantly from that of all cavities (Fig. 8c), and the mean size of critical cavities is larger than that of non-critical cavities. Noticeably, for two closely located cavities of similar shape, degree of isolation and distance from the layer base, the largest cavity is the one associated with joint initiation (e.g. compare critical Cavity 2 and its nearest neighbors to the east at distance 0.7 m along the traverse, Fig. 7). These observations suggest a cavity size effect, whereby larger cavities preferably fail before smaller

Table 2
Estimation of fracture stresses on the Soreq Formation joints

Fractographic method (1)								
K_{Ic}	Q	r/C	C_{cr} (mm)[a]			σ_f (MPa)		
(MPa m$^{1/2}$)			Layer 1	Layer 5	Layer 7	Layer 1	Layer 5	Layer 7
1.66	2.46	16.7	21	30	27	9.1	7.6	8.1
2.47	2.46	16.7	21	30	27	13.5	11.4	12.1
1.66	2.46	13.9	54	36	57	5.2	7.0	5.6
2.47	2.46	13.9	54	36	57	7.8	10.4	8.3
Fractographic method (2)								
G-factor	E (GPa)	γ (J m$^{-1/2}$)	r (m)[a]			σ_f (MPa)		
			Layer 1	Layer 5	Layer 7	Layer 1	Layer 5	Layer 7
$2\sqrt{2}$	30	32	0.90	0.51	0.80	3.2	4.3	3.5
$5\sqrt{2}$	30	32	0.90	0.51	0.80	8.2	10.9	8.7
$2\sqrt{2}$	30	44	0.36	0.51	0.45	6.1	5.1	4.6
$5\sqrt{2}$	30	44	0.36	0.51	0.45	15.2	12.8	13.6

[a] Minimum and maximum values.

ones. This size effect is complicated by post-fracturing dissolution processes that might obliterate the exact cavity size at initiation. Nonetheless, this later dissolution might enlarge all cavities, including the non-critical cavities. Although, theoretically, the SCF of circular hole is 3.0, independent of the size (Lawn, 1993, p. 3), actual strength measurements in rock mechanics experiments indicate that sample strength decreases with increasing hole size (Anderson, 1995, p. 339). Therefore, the SCF effects of the larger hole act over a wider distance, indicating that the volume over which the stress acts is important for hole failure and rock strength. Other studies have also shown that

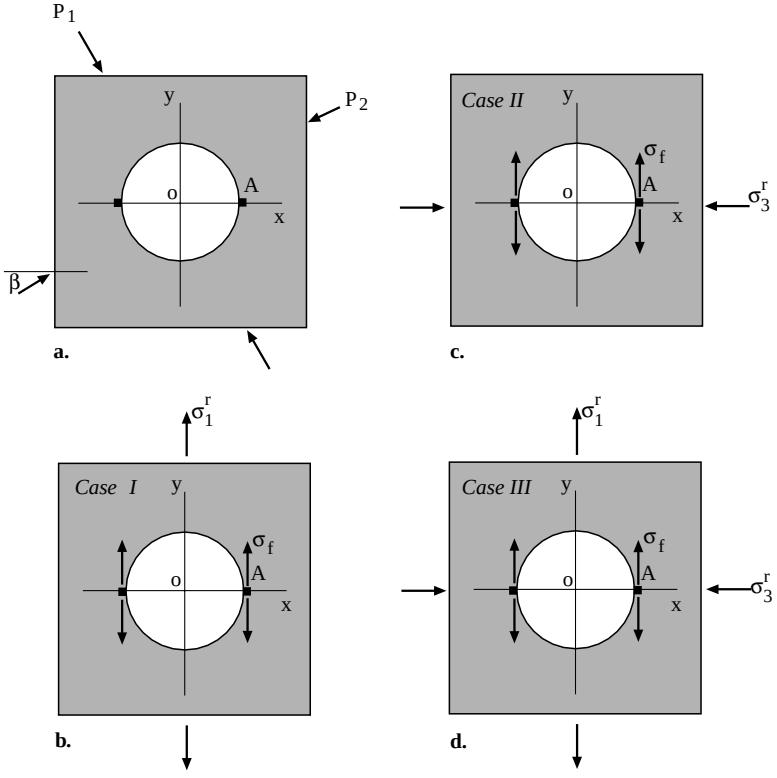

Fig. 10. (a) Circular hole with principal stress p_1 and p_2 at infinity inclined at β and $\pi/2 + \beta$ to the axis Ox, respectively. (b) Circular hole subjected to uniaxial tensile stress, σ_1^r with $\beta = \pi/2$. (c) Circular hole subjected to uniaxial compressive stress, σ_3^r with $\beta = 0$. (d) Circular hole subjected to biaxial stresses. σ_f is the tangential stress at point A along the periphery. The boundary condition at the cavity periphery may be that of constant internal pressure, p. Indicated cases refer to Section 4.5.

rock strength decreases with increasing flaw size and flaw density (Wong et al., 1996; Wong and Chau, 1998; Bazant and Planas, 1998). These size effects, however, are obscured by the fact that they depend on the deformation processes, which in turn depend on the loading conditions (Li et al., 1999). Indeed, in the present case study, only one critical cavity is among the top five largest cavities, indicating that other factors play a more significant role than the size during jointing.

The distribution of cavities in Layer 1 is non-uniform, with cavities clustered toward the layer base. This, in turn, leaves relatively isolated cavities near the middle of the layer, many of which are critical (Fig. 7). For two cavities of similar shape, size and distance from the layer base, the more in-plane isolated cavity is the one associated with joint initiation (e.g. compare Cavity 6 and non-critical cavity at distance 3.45 m along the traverse, Fig. 7). The analysis of the stress in the vicinity of a hole in an elastic material indicates that the stress distribution is markedly affected by the hole only within an area of about three radii from the center of the hole (Timoshenko and Godier, 1951). Thus, closely located cavities may inhibit joint initiation because of the stress perturbation induced by adjacent cavities. On the other hand, in more plausible configurations, cavity-driven joints in less dense regions near the middle of the layer might communicate with other cavities, facilitating joint nucleation caused by stress enhancement.

In cavity-free layers, joints nucleate along bedding interfaces at flaws that cannot be discriminated macroscopically. The common location of joint initiation points along the upper part of layers and, consequently, downward propagation of joints probably indicates that σ_1^r is more compressive downward. Such stress distribution is also consistent with observations that joints in cavity-rich layers originate at cavities located closest to the top. In such cases, the cavities effectively amplified the remote stress such that the tensile strength of the rock is exceeded at the layer interior before it is exceeded at the weak interface above. In the study area, the non-uniform stress distribution could be the result of the regional folding of the Judea Group initiated during Cenomanian–Turonian period (e.g. Bahat, 1999; see Section 5.2). This possibility will be elaborated in a forthcoming paper.

The analysis of joint initiation mechanisms indicates that open cavities are the most severe defects in the dolomite rock masses. The location of joint initiation points is governed by such isolated, relatively large defects, preferably located close to the bedding top, and by stress gradients during joint nucleation.

5.2. Assessments of the paleostress

Several caveats are important when applying the fractographic methods to estimate the fracture stress in the more realistic case of systematic jointing in layered rocks. A joint free of layer-boundary effects will tend to extend along a circular front (Lawn, 1993, pp. 32–33). If a joint does interact with bedding interfaces and adjacent joints and propagates under non-uniform stress distribution, however, its front will deviate from circularity. While a few joints in the Soreq Formation "correct" themselves during propagation and preserve a circular front up to termination, the majorities have an elliptical shape with a subhorizontal major semi-axis away from the initiation point. This front shape records the effect of weak interfaces, which inhibit vertical joint propagation after front intersection and, consequently, cause horizontal straightening of the front. Moreover, interaction with adjacent joints facilitates horizontal propagation up to joint overlapping (e.g. Pollard et al., 1982; Olson and Pollard, 1989), also causing horizontal straightening of the front. This deviation from circularity introduces an error in determination of r (Eqs. (2) and (3)) and, thus, in the estimated fracture stress.

The fractographic methods might also introduce errors into the estimate of fracture stress for joints that initiate at spherical cavities, because the methods account for surface flaws and not strictly for spherical flaws. These errors are probably small, however, because the estimates of fracture stress in a cavity-free layer (Layer 7) are similar to estimates in a cavity-rich layer (Layer 1) (Table 2). Other errors arise from estimating fracture toughness in Eq. (2), and Young's modulus and surface energy in Eq. (3). These variables vary significantly with confining pressure, individual rock types and experimental setting, and between laboratory rock samples and rock masses (e.g. Rubin, 1993). Notwithstanding the close agreement in the values determined using both fractographic methods among different layers (Table 2) and the consistency of these values with experimental data of the Soreq Formation (Section 4.4) suggests that the fracture stress estimates are satisfactory to a first order.

Theoretical arguments indicate that local (true) tension results at the periphery of the spherical cavities. In reality, a small-scale local irregularity (with a high radius of curvature) located along the periphery would produce even higher local tension than calculated in Section 4.4. Thus, the calculations made above are only first-order estimates of the stress required to initiate fractures. It is less clear, however, what is the driving stress needed to promote fracture growth once they propagate out of the tensile field generated by the cavities. The concentric undulations along the joint surfaces are commonly interpreted as an indicative pattern of repeated propagation and arrest (e.g. Engelder and Fischer, 1996), suggesting that cyclic buildup and drop of internal fluid pressure within the cavities and associated joints play an important role during subsequent propagation.

The present study suggests that the remote horizontal least compressive stress σ_1^r is directed N–S, perpendicular to the W-striking joints. This direction approximates the trends suggested by mesostructures (Reches, 1976; Eyal and Reches, 1983; Becker and Gross, 1996; Eyal, 1996), and is probably related to the initial stages of folding during the Cenomanian–Turonian period (Reches, 1976; Bahat,

1999). In this study, however, the observed association between spherical cavities and growth of joints also helps to constrain the magnitude of the remote stress. The estimated magnitudes are related either to cavities that concentrate remote tension or convert remote compression into local tension. The latter case is a likely mechanism for joint nucleation in the Judea Group, if fracturing took place at significant depth.

6. Conclusions

Spherical cavities within the Judea Group function mechanically as macroscopic flaws within dolomite layers. Features of this flaw population are strongly related to diagenetic sedimentary processes, which influence cavity shape, size, orientation, and distribution. The most severe, or critical cavities that serve as initiation points for systematic joints, are typically most closely located to the top of the layers, and are isolated and larger than non-critical cavities. In the absence of macroscopic cavities, joint initiation points are located along bedding interfaces highlighting the important role played by these discontinuities on the nucleation of joints.

Joints typically show two forms of growth, depending on the non-uniform distribution of cavities within the layers. In layers with plentiful cavities, joints propagate vertically toward the bedding interfaces, and horizontally toward adjacent joints, forming elliptical fractures. In layers free of cavities, joints commonly propagate downward toward the layer base and adjacent joints, forming semi-elliptical fractures. In both cases, joints are impeded by bedding interfaces between the dolomite layers, forming arrays of en-échelon joints selectively confined to individual layers. For fluid migration, this architecture provides a less permeable path than continuous planar composite joints.

An assessment of the fracture stress and remote stress by means of surface morphology of joints suggests satisfactory, first order estimation of the paleostress by the fractographic methods. In the Judea Group, the effective conversion of remote compression into local tension by the spherical cavities was the likely mechanism for joint nucleation. Recently, Bai and Pollard (2000) suggest a new mechanism for infilling joints up to saturation that includes joint initiation from flaws with a finite radius of curvature at their extremity. Further field-based studies of cavity-driven joints in the Judea Group should shed more light on this mechanism, and on the association between distribution of cavity-shaped flaws within layered rock and joint spacing and architecture.

Acknowledgements

Discussions with Vladimir Lyakhovsky, Amotz Agnon, Meir Abelson and Dov Bahat motivate this work. Comments and suggestions made by Michael Gross led to significant improvements in the paper. Don Sweetkind, Jim Evans and two anonymous reviewers provided constructive and useful reviews of the manuscript. I gratefully acknowledge the field assistance of Moshe Arnon and the style editing by Ximena Wdowinski. This study was supported by grant No. 9800198 from the United States–Israel Binational Science Foundation (BSF), Jerusalem, Israel.

References

Ameen, M.S. (Ed.), 1995. Fractography: Fracture Topography as a Tool in Fracture Mechanics and Stress Analysis. Geol. Soc. London Spec. Publ. 92, pp. 215–233.

Anderson, T.L., 1995. Fracture Mechanics: Fundamentals and Applications. CRC Press, London.

Arkin, Y., 1989. Moza–Ruppin environmental impact: geology, geotechnics, hydrology. Isr. Geol. Surv. Rep. GSI/58/1989, 32p. (in Hebrew).

Arkin, Y., Hamaoui, M., 1967. The Judea Group (Upper Cretaceous) in central and southern Israel, Isr. Geol. Surv. Bull., 42.

Atkinson, B.K., Meredith, P.G., 1987. The theory of subcritical crack growth with applications to minerals and rocks. In: Atkinson, B.K. (Ed.). Fracture Mechanics of Rock. Academic Press, London, pp. 111–166.

Bahat, D., 1991. Tectonofractography. Springer-Verlag, Berlin.

Bahat, D., 1998. Quantitative tectonofractography—an appraisal. In: Rossmanith, H.P. (Ed.). Mechanics of Jointed and Faulted Rocks. Balkema, Rotterdam, pp. 59–67.

Bahat, D., 1999. On joints and paleostresses associated with folds along the Syrian Arc in the Negev. Isr. J. Earth Sci. 48, 29–36.

Bahat, D., Engelder, T., 1984. Surface morphology on cross-fold joints of the Appalachian Plateau, New York and Pennsylvania. Tectonophysics 104, 299–313.

Bahat, D., Rabinovitch, A., 1988. Palestress determination in a rock by fractographic method. J. Struct. Geol. 10, 193–199.

Bahat, D., Grossenbacher, K., Karasaki, K., 1999. Mechanism of exfoliation joint formation in granitic rocks, Yosemite National Park. J. Struct. Geol. 21, 85–96.

Bai, T., Pollard, D.D., 2000. Fracture spacing in layered rocks: a new explanation based on the stress transition. J. Struct. Geol. 22, 43–57.

Bankawitz, P., 1966. Über klüfte, 2 Die bildung der kluftfläche und eine systematik ihrer strukturen. Geologie 15, 896–941.

Bazant, Z.P., Planas, J., 1998. Fracture and Size Effect in Concrete and Other Quasi-brittle Materials. CRC Press, Boca Raton.

Becker, A., Gross, M.R., 1996. Mechanism for joint saturation in mechanically layered rocks: an example from southern Israel. Tectonophysics 257, 223–237.

Caine, J.S., Forster, C.B., 1999. Fault zone architecture and fluid flow: insights from field data and numerical modeling. In: Haneberg, W.C., Mozley, P.S., Moore, J.C., Goodwin, L.B. (Eds.). Faults and Subsurface Fluid Flow in the Shallow Crust. , pp. 101–128 Geophisical Monograph Series 113, AGU.

Davis, J.C., 1973. Statistical and Data Analysis in Geology. New York, Wiley.

DeGraff, J.M., Aydin, A., 1988. Surface morphology of columnar joints and its significance to mechanics and direction of joint growth. Geol. Soc. Am. Bull. 99, 605–617.

Engelder, T., Fischer, M.P., 1996. Loading configurations and driving mechanisms for joints based on the Griffith energy-balance concept. Tectonophysics 256, 253–277.

Engelder, T., Geiser, P., 1980. On the use of regional joint sets as trajectories of paleostress fields during the development of the Appalachian Plateau, New York. J. Geophy. Res. 85, 6319–6341.

Eyal, Y., 1996. Stress field fluctuations along the Dead Sea rift since the middle Miocene. Tectonics 15, 157–170.

Eyal, Y., Reches, Z., 1983. Tectonic analysis of the Dead Sea rift region since the Late Cretaceous based on mesostructures. Tectonics 2, 167–185.

Friedman, M., Handin, J., Alani, G., 1972. Fracture energy of rocks. Int. J. Rock. Mech. Min. Sci. Geomech. Abstr. 9, 757–766.

Helgeson, D.E., Aydin, A., 1991. Characteristics of joint propagation across layer interfaces in sedimentary rocks. J. Struct. Geol. 13, 897–911.

Kulander, B.R., Barton, C.C., Dean, S.L., 1979. Application of fractography to core and outcrop investigations, United State Department of Energy, paper METL/SP-79/3.

Jaeger, J.C., Cook, N.G.W., 1979. Fundamentals of Rock Mechanics. Chapman and Hall, New York.

Lacazetta, A., Engelder, T., 1992. Fluid-driven cyclic propagation of a joint in the Ithaca siltstone, Appalachian Basin, New York. In: Evans, B., Wong, T.F. (Eds.), Fault Mechanics and Transport Properties of Rocks. Academic Press, London 297–323.

Lawn, B., 1993. Fracture of Brittle Solids. Cambridge University Press, London.

Li, L., Aubertin, M., Simon, R., 1999. Multiaxial failure criterion with time and size effects for intact rock. In: Amadei, et al. (Eds.). Rock Mechanics for Industry. Balkema, Rotterdam, pp. 653–659.

Olson, J.E., Pollard, D.D., 1989. Inferring paleostresses from natural fracture patterns: a new method. Geology 17, 345–348.

Pollard, D.D., Segall, P., Delaney, P.T., 1982. Formation and interpretation of dilatant echelon cracks. Geol. Soc. Am. Bull. 93, 1291–1303.

Pollard, D.D., Aydin, A., 1988. Progress in understanding jointing over the past century. Geol. Soc. Am. Bull. 100, 1181–1204.

Reches, Z., 1976. Analysis of joints in two monoclines in Israel. Geol. Soc. Am. Bull. 87, 1654–1662.

Renshaw, C.R., 1996. Influence of subcritical fracture growth on the connectivity of fracture networks. Water Resour. Res. 32, 1519–1530.

Rubin, A.M., 1993. Tensile fracture of rock at high confining pressure: implications for dike propagation. J. Geophys. Res. 98, 15919–15935.

Sass, E., Bein, A., 1978. Platform carbonates and reefs in the Judean Hills, Carmel and Galilee, Tenth International Congress on Sedimentology Guidebook, pp. 241–274.

Timoshenko, S., Godier, J.N., 1951. Theory of Elasticity. McGraw–Hill, New York.

Weinberger, R., 1999. Initiation and growth of cracks during desiccation of stratified muddy sediments. J. Struct. Geol. 21, 379–386.

Weinberger, R., 2001. Evolution of polygonal patterns in stratified mud during desiccation: the role of flaw distribution and layer boundaries. Geol. Soc. Am. Bull. 113, 20–31.

Weinberger, R., Reches, Z., Eidelman, A., Scott, T.E., 1994. Tensile properties of rocks in four-point beam tests under confining pressure. In: Nelson, P., Laubach, S.E. (Eds.). Rock Mechanics Models and Measurements Challenges from Industry. Balkema, Rotterdam, pp. 435–442.

Wong, R.H.C., Chau, K.T., 1998. Peak strength of replicated and real rocks containing cracks. Trans Tec Publications, pp. 953–958 Key Engineering Materials, 145–149.

Wong, R.H.C., Chau, K.T., Wang, P., 1996. Microcracking and grain size effect in Yuen Kong marbles. Int. J. rock Mech. Min. Sci. Geomech. Abstr. 33 (5), 479–485.

Wong, T.-F., Zhu, W., 1999. Brittle faulting and permeability evolution: hydromechanical measurements, microstructural observation, and network modeling. In: Haneberg, W.C., Mozley, P.S., Moore, J.C., Goodwin, L.B. (Eds.). Faults and Subsurface Fluid Flow in the Shallow Crust, pp. 101–128 Geophisical Monograph Series 113, AGU.